An efficient photoelectric X-ray polarimeter for the study of black holes and neutron stars

Enrico Costa*, Paolo Soffitta*, Ronaldo Bellazzini†, Alessandro Brez†, Nicholas Lumb† & Gloria Spandre†

** Istituto di Astrofisica Spaziale del CNR, Via Fosso del Cavaliere 100, 1-00133, Rome, Italy*

† Istituto Nazionale di Fisica Nucleare-Sezione di Pisa, Via Livornese 1291, I-56010 San Piero a Grado, Pisa, Italy

The study of astronomical objects using electromagnetic radiation involves four basic observational approaches: imaging, spectroscopy, photometry (accurate counting of the photons received) and polarimetry (measurement of the polarizations of the observed photons). In contrast to observations at other wavelengths, a lack of sensitivity has prevented X-ray astronomy from making use of polarimetry. Yet such a technique could provide a direct picture of the state of matter in extreme magnetic and gravitational fields[1–6], and has the potential to resolve the internal structures of compact sources that would otherwise remain inaccessible, even to X-ray interferometry[7]. In binary pulsars, for example, we could directly 'see' the rotation of the magnetic field and determine if the emission is in the form of a 'fan' or a 'pencil' beam[1,8]. Also, observation of the characteristic twisting of the polarization angle in other compact sources would reveal the presence of a black hole[9–12]. Here we report the development of an instrument that makes X-ray polarimetry possible. The factor of 100 improvement in sensitivity that we have achieved will allow direct exploration of the most dramatic objects of the X-ray sky.

The main advantage of the proposed polarimeter is its capability of investigating active galactic nuclei (quasars, blazars and Seyfert galaxies) for which polarization measurements have been suggested, crucial to understand the geometry and physics of emitting regions. We can separate synchrotron X-rays from jets[13,14] from the emission scattered by the disk corona or by a thick torus. The effects of relativistic motions and of the gravitational field of a central black hole have probably been detected by iron line spectroscopy on the Seyfert-1 galaxy MCG-6-30-15 (ref. 15) but this feature is not ubiquitous in active galactic nuclei. Polarimetry of the X-ray continuum provides a more general tool to explore the structure of emitting regions[16,17], to track instabilities and to derive direct information on mass and angular momentum[12] of supermassive black holes.

In spite of this wealth of expectations, the important but only positive result until now is the measurement, by the Bragg technique, of the polarization of the Crab nebula[18,19]. The Stellar X-ray Polarimeter[20] (SXRP) represents the state of the art for conventional methods based on Bragg diffraction and Thomson scattering. However, Bragg polarimetry[21] is dispersive (one angle at one time) and very narrow-band. Thomson polarimetry[22] is non-imaging and band-limited (>5 keV). This limits the sensitivity of SXRP to a few bright, galactic sources only.

The photoelectric effect is very sensitive to polarization. The electron is ejected from an inner shell with a kinetic energy which is the difference between the photon energy and the binding energy. The direction of emission is not uniform but is peaked around that of the electric field of the photons (see Fig. 1a). This photoelectron

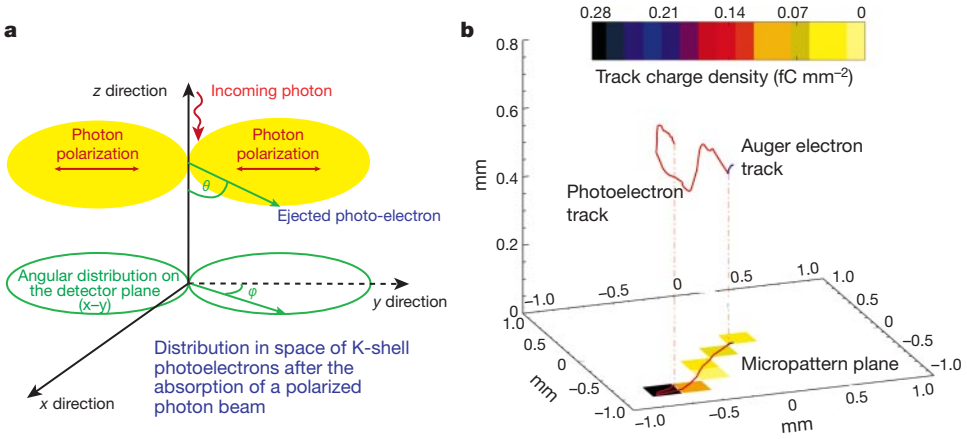

Figure 1 Basic physics of the photoelectric effect in a gas. **a**, Following the photon conversion in the gas, the photoelectron is ejected in directions that carry a significant memory of the electric field of the photon. When the beam is linearly polarized the electrons are ejected preferentially around the electric field. The cross-section of s electrons is:

$$\frac{\partial\sigma}{\partial\Omega} = r_0^2 \frac{Z^5}{137^4}\left(\frac{mc^2}{h\nu}\right)^{7/2} \frac{4\sqrt{2}\sin^2(\theta)\cos^2(\varphi)}{(1-\beta\cos(\theta))^4}$$

where r_0 is the classical electron radius, Z is the atomic number of the target material and β is the electron velocity, as a fraction of the speed of light c. The figure shows the emission angle θ and azimuth angle φ. **b**, A simulated 6-keV photoelectron and Auger track, showing propagation in the gas and collection on a plane with sensitivity to both energy and position. The photoelectron is slowed by ionizing collisions with outer electrons of the atoms of the medium. The energy loss increases with decreasing kinetic energy (Bethe law for low energy).

$$\frac{\partial E}{\partial x} \propto \frac{1}{\beta^2} \propto \frac{1}{E_{kin}}$$

Electrons are also scattered by charges in the nuclei with no significant energy loss. This follows the screened Rutherford law:

$$\frac{\partial\sigma}{\partial\Omega} \propto \frac{Z^2/E_{kin}^2}{(\sin^2(\vartheta/2)+\alpha_{screen})^2}$$

Whereas scattering crucially depends on the atomic number, slowing down is only moderately dependent. The primary ionizations are then projected onto the sense plane. The charge density in each pixel is proportional to the energy loss, and is therefore related to the electron kinetic energy. The first part of the photoelectron path has a lower charge density, but it is closer to the initial direction of the photoelectron and so also closely related to the photon polarization direction. The second part has a higher charge density but it is randomized. The Auger electron track does not bring information on polarization.

interacts with the surrounding matter: it is slowed by ionizing collisions with atomic electrons and scattered by Coulomb diffusion on the nuclei (see Fig. 1b) and eventually stopped. The photoelectron leaves a string of electron–ion pairs in the absorber, marking the path from its creation to the stopping point. We call this string a 'track': in the initial part of this track resides the information on the original electron direction from which the polarization of the photon may be derived. This dependence is preserved if the track is projected onto a plane perpendicular to the radiation.

In a subdivided detector extended tracks may produce coincident signals in two contiguous cells. If the radiation is polarized the orientation of these pairs is asymmetric. We can exploit this by counting coincidences in neighbouring wires of proportional counters[23] or charge-coupled device (CCD) pixels[24,25]. But as the detector cell is typically much larger than the electron range, the asymmetry effect strongly depends on the absorption point. This can be avoided if the cell is so small that the track is split into several cells. The first finely subdivided, self-triggered device[26] was a micro-gap[27] chamber filled with a neon-based gas mixture at 1 atm. The need to rotate the instrument and an as yet moderate modulation factor mean that this device is a step forward, but not by much.

Other instruments image the bright track made in a gas scintillation detector on a CCD. One of the two practical implementations[28] works only above 40 keV, the other[29] only at low pressure. Both use argon which, because of the higher energy of the isotropic Auger electron and larger multiple scattering, is a gas suitable for photon energies higher than the practical range for X-ray optics.

Position-sensitive gas detectors typically yield the centroid of the charge cloud, whose extent is the ultimate limit to the space resolution, a sort of noise to be kept as small as possible. We reverse this approach, trying to resolve the track to measure the interaction point and the prime direction of the photoelectron. To this end we have developed the micro-pattern gas chamber (MPGC). It consists (Fig. 2, Table 1) of a gas cell with a thick detection/drift region, a thin gas electron multiplier (GEM[30]) and a multi pixel, true two-dimensional, read-out anode. The large number of fired pixels per track allows for a good track reconstruction. Additionally, the MPGC measures the energy lost in each pixel, a quantity directly related to the kinetic energy of the electron.

We filled the MPGC with a 1-atm mixture of Ne (80%)-dimethyl-ether (DME; 20%). Figure 3a shows the image of a real MPGC track. An initial straighter part, with low ionization density, which carries

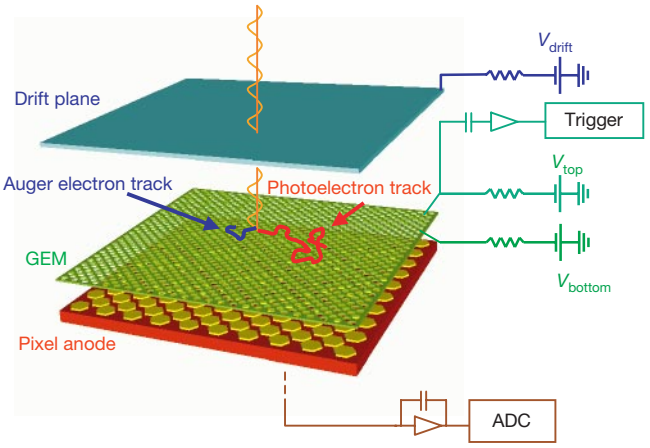

Figure 2 The micro-pattern gas detector. The photon is absorbed at some point in the drift gap. The photoelectron track is drifted by the electric field to the gas electron multiplier (GEM). This device is made of a thin (50 μm) polyimide foil perforated by many microscopic holes, where a high electric field provides the charge amplification. Finally, the charge is collected by the pixels of MPGC anode, each one connected to an independent electronics chain. On receiving a trigger from the GEM, all the signals are converted from analog to digital, so that we have the image of the track projected on the detector plane.

most of the information on the starting direction (and thence on the polarization) evolves into a skein with high ionization density and a completely random path. Most of the photoelectron energy is lost at some distance from the initial interaction point. To verify this interpretation we let impinge on the detector, through a very thin diaphragm, photons of 5.4 keV from an unpolarized source. The loci of the centroids of each track are displaced from the interaction point and located on a circular region around it, indicating that the tracks have, and retain, a significant elongation and energy loss asymmetry (Fig. 3b). From each track we reconstructed the emission angle and we built a histogram. In the case of unpolarized X-ray photons of 5.4 and 5.9 keV, all the emission angles have the same probability and the histogram is flat (Fig. 3b). When we irradiated the detector with an extended, nearly 100% polarized source of 5.4 keV, we found a strong angular modulation (44%) that is well modelled by the expected distribution (Fig. 3c), taking into account

Table 1 Physical characteristics and performances of the micro-pattern detector

	Present prototype (2–10 keV)	Improved configuration (3.5–10 keV)
Drift/absorption gap	6 mm	30 mm
Drift field	3,000 V cm^{-1}	1,500 V cm^{-1}
Gas filling and pressure	(Ne 80%–DME 20%); 1 atm	(Ne 40%–DME 60%); 4 atm
Gas grain	5,000	2,500
Transverse diffusion in drift	80 μm	<100 μm
GEM thickness	50-μm copper-clad kapton foil	50-μm copper-clad kapton foil
GEM hole geometry	40-μm diameter; 60-μm pitch	40-μm diameter; 60-μm pitch
GEM voltage	400 V	600 V
Detection efficiency at 5.4 keV	3.8%	91%
Read-out pixel size	200 μm	50 μm
Number of pixels	512	40,000
Read-out plane technology	Multilayer advanced PCB	VLSI
Track length/pixel size (6 keV)	6	6
Sensitivity to Her X1	$T = 400$ s; MDP = 10%	$T = 20$ s; MDP = 10%
Sensitivity to 3C-273	$T = 2.2 \times 10^5$ s; MDP = 2%	$T = 4 \times 10^4$ s; MDP = 1%
Sensitivity to MCG-6-30-15	$T = 5 \times 10^5$ s; MDP = 2%	$T = 1 \times 10^5$ s; MDP = 1%
Gain in the integration time over SXRP (strong sources)	5 (over Thomson); 15 (over Bragg)	100 (over Thomson); 300 (over Bragg)
Gain in the integration time over SXRP (faint sources)	250 (over Thomson); 100 (over Bragg)	5,000 (over Thomson); 2,000 (over Bragg)

We show also the observing time needed to measure (at 99% confidence) the shown degree of polarization (minimum detectable polarization or MDP) of a selected sample of astrophysical sources if the micro-pattern gas chamber (MPGC) is placed at the focus of the SODART[33] telescope on board the Spectrum X-gamma mission. The relevant formalism can be found in ref. 26. For the improved design we use only photons above 3.5 keV to compute the sensitivity. Below this energy, at high pressure, the transverse diffusion and the unfavourable track length to pixel size ratio significantly reduces the modulation. Her X-1 is a galactic binary X-ray source with a magnetic field of about 3.5×10^{12} G measured by the detection of a cyclotron line. A high degree of linear polarization is expected and, by polarimetry, a direct measure of the angle between the magnetic field and the rotation axis with 1° accuracy can be performed. 3C-273 is the X-ray brightest radio-loud quasar and MCG-6-30-15 is a Seyfert-1 galaxy for which a broad (~80.000 km s^{-1}) iron line was observed, possibly skewed by gravitational effects[15]. Finally, we compare the performances of MPGC with SXRP, the most sensitive polarimeter foreseen in a future X-ray mission, ready to be installed in the focal plane of the SODART telescope. It simultaneously exploits the Bragg diffraction at 45° and the azimuth dependence on polarization of Thomson scattering. The ensemble analyser/detector of the two stages is rotated to search for a modulation in the counting rate and to compensate for systematic effects. GEM, gas electron multiplier. VLSI, very large scale integration; PCB, printed circuit board; DME, dimethylether.

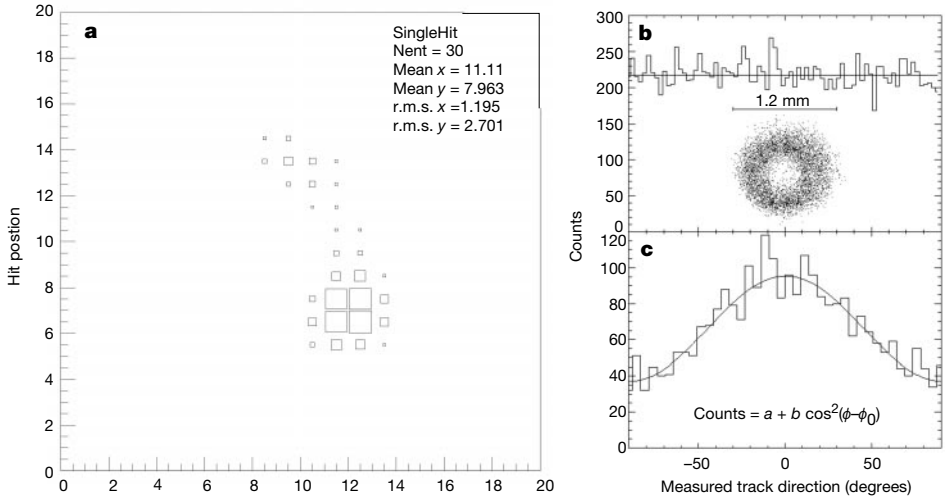

Figure 3 The polarization angle measurement. **a**, Image of a real photoelectron track detected by an MPGC filled with neon (80%) and dimethylether (20%). Scale unit is pixel number and larger boxes correspond to a larger energy loss. Each pixel is 200 μm wide. It is possible to recognize the beginning of the track with the Auger electron followed by the weaker ionization loss of the photoelectron (top) and the end of the track with a much larger energy loss (70% of the total charge for this specific event, bottom). For each photoelectron it is, therefore, possible to measure the initial direction of the track, which carries the memory of the polarization. By reconstructing the impact point of the photon, the real position resolution is much better than that imposed by the track extension and is only a factor of two or three worse than a charge-coupled device (CCD). **b**, **c**, Histograms of the emission angles of the photoelectron in the detector plane as reconstructed from data like those of **a**. **b**, Unpolarized photons from a Fe^{55} source. No preference in the track direction results in a histogram which is consistent with a flat curve. The loci of the baricentres for a 5.4-keV pencil beam of unpolarized photons are displayed, showing how tracks retain their energy loss asymmetry. **c**, Nearly 100% polarized photons from a 5.4-keV extended source. The amplitude of the $\cos^2$ fit to the histogram of counts is directly related to the sensitivity of a real polarimeter. The angular phase is the direction of polarization of the incoming photons. The so called modulation factor $(C_{max} - C_{min})/(C_{max} + C_{min})$ is measured to be 0.44. The χ^2_{red} to the fit is 1.02; $a = 36.98 \pm 1.84$; $b = 58.43 \pm 3.57$; $\phi_0 = 0.45° \pm 1.73°$.

the theoretical distribution of the photoelectron and the smearing due to scattering.

We chose a Ne-based gas mixture to fill the gas chamber because in the energy band of interest the photoelectron track is longer and fires several pixels, while retaining reasonable efficiency. A low-atomic-number gas is less efficient for detection of primary photons. However, the scattering/slowing ratio is lower as well: the track is straighter and the direction of emission can be measured more precisely. Moreover the Ne K-edge energy is so low (0.87 keV) that the accompanying isotropic Auger electron does not blur the information on the polarization; in fact, it makes the identification of the impact point easier. The use of even lower K-edge converters together with a very fine pixel size could make low-energy polarimeters (0.5–2 keV) possible.

With our prototype we have demonstrated the practical feasibility of a new generation of photoelectric polarimeters in the 2–10 keV band. The device can simultaneously also produce good images (50–100 μm), moderately good spectroscopy (16% full-width at half-maximum, at 5.4 keV), and fast, high-rate timing down to 150 eV. Moreover, being truly two-dimensional, it is non-dispersive and does not require rotation.

We also tested our capability to model the polarization detection processes. As absorption, slowing down, scattering and transverse diffusion of electrons in the drift are well known quantities, we may reliably predict the performance of another detector configuration that would be better optimized for astrophysical applications. It is based on an existing[31] VLSI (Very Large Scale Integration) readout chip combined with other well established detector technology. We can derive the polarimetric sensitivity of such detectors when installed at the focus of a real X-ray telescope. In Table 1 we compare the sensitivity of the present and final configuration of the MPGC with SXRP.

The MPGC requires integration periods that are about 100 times shorter than those of the SXRP to detect the same polarization in bright sources. With integrations of the order of one day we could perform polarimetry of active galactic nuclei at the 1% level, a breakthrough in this fascinating window of high-energy astrophysics. With the planned XEUS[32] telescope, polarimetry could become a new high-throughput branch of X-ray astronomy. □

Received 23 January; accepted 2 April 2001.

1. Mészáros, P., Novick, R., Chanan, G. A., Weisskopf, M. C. & Szentgyörgyi, A. Astrophysical implication and observational prospects of X-ray polarimetry. *Astrophys. J.* **324,** 1056–1067 (1988).
2. Rees, M. J. Expected polarization properties of binary X-ray sources. *Mon. Not. R. Astron. Soc.* **171,** 457–465 (1975).
3. Sunyaev, R. A. & Titarchuk, L. G. Comptonization of low-frequency radiation in accretion disks: angular distribution and polarization of hard radiation. *Astron. Astrophys.* **143,** 374–388 (1985).
4. Gnedin, Yu. N., Pavlov, G. G. & Shibanov, Yu. A. The effect of vacuum birefringence in a magnetic field on the polarization and beaming of X-ray pulsars. *Sov. Astron. Lett.* **4,** 117–119 (1978).
5. Ventura, J. Scattering of light in strongly magnetized plasma. *Phys. Rev. D* **19,** 1684–1695 (1979).
6. Mészáros, P. & Ventura, J. Vacuum polarization effects on radiative opacities in strong magnetic field. *Phys. Rev. D* **19,** 3565–3575 (1979).
7. Cash, W., Shapley, A., Osterman, S. & Marshall, J. Laboratory detection of X-ray fringes with grazing-incidence interferometer. *Nature* **407,** 160–162 (2000).
8. Gnedin, Yu. N. & Sunyaev, R. A. Polarization of optical and X-ray radiation from compact thermal sources with magnetic field. *Astron. Astrophys.* **36,** 379–394 (1974).
9. Connors, P. A. & Stark, R. F. Observable gravitational effects on polarized radiation coming from near a black hole. *Nature* **269,** 128–129 (1977).
10. Stark, R. F. & Connors, P. A. Observational test for the existence of a rotating black hole in Cyg X-1. *Nature* **266,** 429–430 (1977).
11. Connors, P. A., Piran, T. & Stark, R. Polarization features of X-ray radiation emitted near a black hole. *Astrophys. J.* **235,** 224–244 (1980).
12. Bao, G., Wiita, P. & Hadrava, P. Energy-dependent polarization variability as a black hole signature. *Phys. Rev. Lett.* **77,** 12–15 (1996).
13. Celotti, A. & Matt, G. Polarization properties of synchrotron self-Compton emission. *Mon. Not. R. Astron. Soc.* **268,** 451–458 (1994).
14. Poutanen, J. Relativistic jets in blazars: polarization of radiation. *Astrophys. J. Suppl. Ser.* **92,** 607–609 (1994).
15. Tanaka, Y. *et al.* Gravitationally redshifted emission implying an accretion disk and massive black-hole in the active galaxy MCG-6-30-15. *Nature* **375,** 659–661 (1995).
16. Ogura, J., Nobuyori, O. & Kojima, Y. Profiles and polarization properties of emission lines from relativistic disks. *Publ. Astron. Soc. Jpn* **52,** 841–845 (2000).
17. Matt, G., Fabian, A. C. & Ross, R. R. X-ray photoionized accretion discs: UV and X-ray continuum spectra and polarization. *Mon. Not. R. Astron. Soc.* **264,** 839–852 (1993).
18. Novick, R., Weisskopf, M. C., Berthelsdorf, R., Linke, R. & Wolff, R. S. Detection of X-ray polarization of the Crab Nebula. *Astrophys. J.* **174,** L1–L8 (1972).
19. Weisskopf, M. C., Silver, E. H., Kestenbaum, H. L., Long, K. S. & Novick, R. A precision measurement of the X-ray polarization of the Crab Nebula without pulsar contamination. *Astrophys. J.* **220,** L117–L122 (1978).
20. Kaaret, P. *et al.* SXRP: a focal plane stellar X-ray polarimeter for the Spectrum-X-Gamma mission. *Opt. Eng.* **29,** 773–783 (1990).
21. Schnopper, H. W. & Kalata, K. Polarimeter for celestial X-rays. *Astron. J.* **74,** 854–858 (1969).
22. Novick, R. in *Planets, Stars and Nebulae Studied with Photopolarimetry* (ed. Gerehls, T.) 262–317 (Univ. Arizona Press, Tucson, 1972).

23. Riegler, G. R., Garmire, G. P., Moore, W. E. & Stevens, J. A low-energy X-ray polarimeter. *Bull. Am. Phys. Soc.* **15,** 635 (1970).
24. Tsunemi, H. *et al.* Detection of X-ray polarization with a charge coupled device. *Nucl. Instrum. Methods A* **321,** 629–631 (1992).
25. Buschhorn, G. *et al.* X-ray polarimetry using the photoeffect in a CCD detector. *Nucl. Instrum. Methods A* **346,** 578–588 (1994).
26. Soffitta, P. *et al.* Astronomical X-ray polarimetry based on photoelectric effect with microgap detectors. *Nucl. Instrum. Methods A* (in the press); also preprint astro-ph/0012183 at ⟨xxx.lanl.gov⟩ (2000).
27. Angelini, F. *et al.* The micro-gap chamber. *Nucl. Instrum. Methods A* **335,** 69–77 (1993).
28. Austin, R. A., Minamitani, T. & Ramsey, B. Development of a hard X-ray imaging polarimeter. *Proc. SPIE* **2010,** 118–125 (1993).
29. La Monaca, A. *et al.* A new photoelectron imager for X-ray astronomical polarimetry. *Nucl. Instrum. Methods A* **416,** 267–277 (1998).
30. Sauli, F. GEM: a new concept for electron amplification in gas detectors. *Nucl. Instrum. Methods A* **386,** 531–534 (1997).
31. Campbell, M. *et al.* A pixel readout chip for 10–30 Mrad in standard 0.25 μm CMOS. *IEEE Trans. Nucl. Sci.* **46,** 156–160 (1999).
32. Bavdaz, M. *et al.* Status of the X-ray evolving universe spectroscopy mission (XEUS). *Proc. SPIE* **4138,** 69–78 (2000).
33. Christensen, F. E. *et al.* X-ray calibration of the SODART flight telescope. *Proc. SPIE* **3113,** 69–78 (1997).

Acknowledgements

This work is partially supported by the Italian Space Agency (ASI).

Correspondence and requests for materials should be addressed to E.C. (e-mail: costa@ias.rm.cnr.it).

Fabry–Perot interference in a nanotube electron waveguide

Wenjie Liang*†, Marc Bockrath†‡, Dolores Bozovic‡, Jason H. Hafner*, M. Tinkham‡ & Hongkun Park*

** Department of Chemistry and Chemical Biology and ‡ Department of Physics, Harvard University, Cambridge, Massachusetts 02138, USA*
† These authors contributed equally to this work

The behaviour of traditional electronic devices can be understood in terms of the classical diffusive motion of electrons. As the size of a device becomes comparable to the electron coherence length, however, quantum interference between electron waves becomes increasingly important, leading to dramatic changes in device properties[1–8]. This classical-to-quantum transition in device behaviour suggests the possibility for nanometer-sized electronic elements that make use of quantum coherence[1,2,7,8]. Molecular electronic devices are promising candidates for realizing such device elements because the electronic motion in molecules is inherently quantum mechanical[9,10] and it can be modified by well defined chemistry[11–13]. Here we describe an example of a coherent molecular electronic device whose behaviour is explicitly dependent on quantum interference between propagating electron waves—a Fabry–Perot electron resonator based on individual single-walled carbon nanotubes with near-perfect ohmic contacts to electrodes. In these devices, the nanotubes act as coherent electron waveguides[14–16], with the resonant cavity formed between the two nanotube–electrode interfaces. We use a theoretical model based on the multichannel Landauer–Büttiker formalism[17–19] to analyse the device characteristics and find that coupling between the two propagating modes of the nanotubes caused by electron scattering at the nanotube–electrode interfaces is important.

Isolated single-walled nanotubes (SWNTs) were synthesized by chemical vapour deposition[13], and electrical devices based on individual SWNTs were fabricated as reported previously using electron-beam lithography[13]. More than 100 nanotube devices have been made and classified as metallic or semiconducting on the basis of their resistance versus gate voltage (V_g) behaviour[13,20]. Most metallic nanotube devices exhibited room-temperature resistance below 100 kΩ, and more than 20 devices exhibited resistance below 15 kΩ. The lowest resistance values observed in some metallic nanotube devices were around 7 kΩ, approaching the theoretical lower limit of 6.5 kΩ for a nanotube device with perfect ohmic contacts[2,14,21]. This observation indicates that the contacts between nanotubes and the Au/Cr electrodes in our nanotube devices are nearly perfect, unlike those in previous SWNT devices[13,16,21–24], and that electrons can pass through the nanotube–metal junction with little reflection. The following discussion concentrates on metallic nanotube devices with room-temperature resistances below 15 kΩ.

Figure 1 shows a differential conductance ($\partial I/\partial V$)–V_g plot near zero bias ($V = 0$) obtained from a representative nanotube device at a temperature $T = 4$ K. The length of the nanotube segment (L) between two electrodes was around 200 nm, as determined by atomic force microscopy. Below $T = 10$ K, the device exhibits pronounced $\partial I/\partial V$ oscillations that are quasi-periodic in V_g with an average conductance of around 3.2 e^2/h (the value of e^2/h is 38.8 μS or (25.8 kΩ)$^{-1}$). Figure 2 shows two-dimensional $\partial I/\partial V$ plots as a function of V and V_g obtained from nanotube devices with $L \approx 530$ nm and $L \approx 220$ nm, respectively. The dips in $\partial I/\partial V$ appear as dark lines in Fig. 2. The positions of the $\partial I/\partial V$ dips evolve smoothly as V and V_g change, forming a mesh of crisscrossing dark lines. Similar $\partial I/\partial V$–V–V_g patterns were observed in 10 other devices with average conductance above $2e^2/h$, although the V and V_g spacing between adjacent dark lines changed from device to device. The conductance behaviour of these devices did not change substantially as the temperature was reduced from 4 K to 100 mK.

Figures 1 and 2 illustrate several characteristics shared by all 12 nanotube devices that exhibit $\partial I/\partial V$ oscillations. The average values of $\partial I/\partial V$ were around 2–3 e^2/h, and $\partial I/\partial V$ remained above e^2/h irrespective of V, V_g and T, clearly indicating that the electrical behaviour of these nanotube devices is distinct from those reported

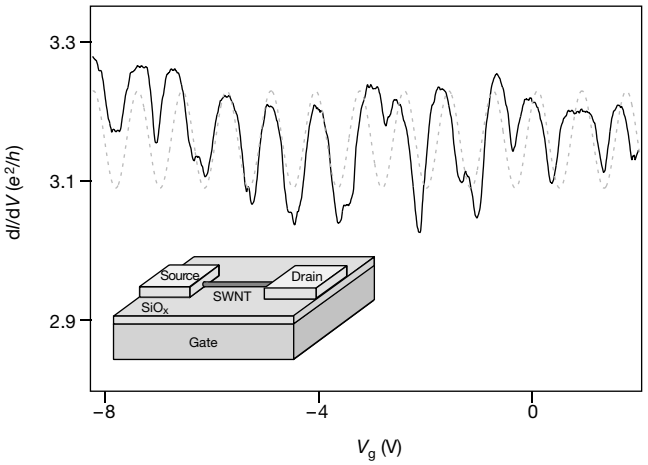

Figure 1 Zero-bias differential conductance ($\partial I/\partial V$) of a 200-nm SWNT device plotted against gate voltage (V_g). Isolated SWNTs were synthesized on a degenerately doped silicon wafer with a 1-μm oxide layer by chemical vapour deposition. Individual SWNTs with ~1-nm height were located by atomic force microscopy, and nanotube devices were fabricated by defining two Au/Cr electrodes on top of the SWNTs by electron-beam lithography. Electrical properties of nanotube devices were characterized as a function of bias voltage (V) and V_g. The degenerately doped silicon substrate was used as a gate electrode to modulate the charge density and the Fermi-level position within the nanotubes. The dotted curve shows a sinusoidal function with the same average period as the measured data. Comparison between these two plots shows that the measured data is quasi-periodic in V_g. Inset, a schematic diagram of the SWNT device, showing a nanotube with attached leads, the insulating gate oxide and the degenerately doped silicon gate.